Passivation Layer Formation of Magnesium Metal Negative Electrodes for Rechargeable Magnesium Batteries

Kuwata, Hiroko

Matsui, Masaki

Imanishi, Nobuyuki

Passivation layer formation of magnesium metal negative electrodes for rechargeable magnesium batteries

Hiroko Kuwata[1], Masaki Matsui[1, 2, 3*] and Nobuyuki Imanishi[1]

1. Department of Chemistry, Mie University
   1577 Kurimamachiya-cho Tsu, 514-8507, Mie, JAPAN
2. Department of Chemical Science and Engineering, Kobe University
   1-1 Rokkodai-cho, Nada-ku, Kobe, 657-8501, Hyogo, JAPAN
3. Japan Science and Technology Agency, PRESTO
   4-1-8 Honcho, Kawaguchi, Saitama 332-0012, Japan

Corresponding Author: Masaki Matsui
Affiliation: Department of Chemical Science and Engineering, KOBE University
phone & fax: +81-78-803-6160
e-mail: matsui@godzilla.kobe-u.ac.jp

Abstract

A comparative study for electrodeposited magnesium metal was conducted using an organohaloaluminate-based electrolyte solution and a conventional ionic electrolyte solution. The deposition / dissolution process of the magnesium metal in the ionic electrolyte solution shows high overpotential with low coulombic efficiency, compared with the organohaloaluminate-based electrolyte solution. The magnesium metal deposited in the ionic electrolyte solution shows porous morphology and poor crystallinity. An initial electrolytes decomposition process on Pt substrate was analyzed with *in situ* FTIR. The *in situ* FTIR spectra show passivation process of the electrode during the 1st cathodic scan due to the decomposition of the conventional ionic electrolyte solution. The surface layer on magnesium metal was characterized by using XPS. The XPS spectra for the magnesium metal immersed in the ionic electrolyte solution proved that a MgF_2-based passivation layer corresponding to the decomposed TFSA anion is formed.

1. Introduction

Electrochemical deposition and dissolution processes of less noble metals, such as lithium, sodium and magnesium, is considered as ideal negative electrode reactions for rechargeable batteries, because their theoretical capacities are much higher than insertion-type of active materials such as graphite[1] and $Li_4Ti_5O_{12}$[2]. One of the biggest challenges of the metal anodes is maintaining smooth surface morphologies during the charging-discharging process. In the case of lithium metal, the dendritic growth during the charging process has been hindering the commercialization of rechargeable lithium batteries, because the dendritic lithium leads short circuit of the cell, creating a fire hazard[3]. In addition, the dendritic lithium easily loses the electrical connection with the anode current collector, which results in significant capacity fade. On the other hand, the magnesium metal does not usually form the dendrite under the same condition of lithium deposition[4-6]. Even though the specific capacity of the magnesium metal is lower than that of the lithium metal, the magnesium metal has an attractive volumetric capacity. The capacity density of the magnesium metal is 3833 $mAh \cdot cm^{-3}$, while that of the lithium metal is 2061 $mAh \cdot cm^{-3}$. Therefore, the magnesium metal is a promising

anode material for beyond lithium-ion batteries.

There still remains a lot of challenges in utilization of the magnesium metal as a negative electrode, especially the choice of the electrolyte solution is critical to develop a practical battery system. The conventional ionic electrolyte solutions, such as magnesium perchlorate (ClO_4^-) or magnesium hexafluorophosphate (PF_6^-) dissolved in carbonate-based solvents, inhibits the reversible deposition / dissolution of the magnesium metal, because a passivation layer is easily formed at the surface of the electrode [7, 8]. Therefore, the electrolyte design to avoid the formation of the passivation layer is necessary to utilize the advantage of the magnesium metal anode.

Grignard reagent such as ethyl magnesium bromide in tetrahydrofuran (THF), is well known as an electrolyte solution for reversible magnesium deposition from 1920s'[9], however the Grignard reagent is not practical for the battery applications due to its narrow electrochemical window. In late 1990s' and 2000s', Aurbach *et al.* developed series of organohaloaluminate-based electrolyte solutions, which show improved electrochemical stabilities[5, 7, 8, 10-13]. They demonstrated the very 1st prototype of the rechargeable magnesium battery using Mo_6S_8 Chevrel phase as a cathode active material[10]. The

organohaloaluminate-based electrolyte solutions are typically prepared by mixing Grignard reagent and alkyl aluminum halides. With optimized composition, these electrolyte solutions show excellent reversibility and wide potential window > 3V[14, 15]. Kim et al. proved that the electrochemical active species in the organohaloaluminate-based electrolyte solution is magnesium dimer complex[16, 17]. Even with the electrochemical window, the organohaloaluminate-based electrolytes have corrosive properties at high electrode potential due to the halides contained in the structure[17, 18]. These corrosive properties make it difficult to use high voltage cathode, due to the increased risk of transition metal dissolution. Thus, it is very crucial to explore another electrolyte solution which has wide electrochemical window without corrosive properties.

Recently conventional ionic electrolyte solutions using magnesium bis(trifluoromethansulfonyl)amide: $Mg(TFSA)_2$ dissolved in ether-based solvents are discovered as alternate electrolyte solutions for the magnesium metal anode[19-21]. Ha *et al.* reported that corrosion of stainless steel and aluminum foil can be inhibited in $Mg(TFSA)_2$-based ionic electrolyte solutions[20], however, limitations still exist. The reported electrochemical properties of the ionic electrolyte solutions are not as good as

that of the organohaloaluminate-based electrolyte solutions. The ionic electrolyte solutions show very high over potential >1.0 V and poor coulombic efficiency < 60% at room temperature, suggesting that some side reaction is taking place besides the electrochemical deposition / dissolution of the magnesium metal, resulting in the partial passivation of the electrode surface.

In the present study, we carried out a comparative study of the electrochemical deposition processes of magnesium metal in an organohaloaluminate-based electrolyte solution and a $Mg(TFSA)_2$-based electrolyte solution. We mainly focused on the characterization of the surface layer using *in situ* FTIR and XPS, and discussed the key parameter for the smooth deposition / dissolution process of the magnesium metal.

2. Experimental

2-1. *Preparation of the Electrolyte solutions*

In the present study, an organohaloaluminate-based electrolyte solution: 0.25 M EtMgCl-2Et_2AlCl in THF (EAC electrolyte solution) and an ionic electrolyte solution: 0.5 M $Mg(TFSA)_2$ in butyl methyl triglyme (BuMeG3 electrolyte solution) were prepared. The EAC electrolyte solution was prepared by mixing a 2 M EtMgCl in THF (Sigma Aldrich), Et_2AlCl (Nippon Aluminum Alkyls) and anhydrous THF (Sigma Aldrich). The BuMeG3 electrolyte solution is prepared by dissolving the $Mg(TFSA)_2$ salt (Kishida) in BuMeG3 (Wako). The chemicals used for the EAC electrolyte solution were used without further purification. On the other hand, the chemicals for the BuMeG3 electrolyte solutions were well dried before usage; the $Mg(TFSA)_2$ was dried under vacuum at 170 ºC for 8 hours. The BuMeG3 was dried with an activated molecular sieve to reduce the water content < 30 ppm. The water content of the BuMeG3 electrolyte solution was determined by Karl Fischer method.

2-2. *Electrochemical Measurements*

Cyclic voltammetries were executed using a three-electrode cell shown in Fig.1. A platinum foil (Nilaco) was employed for the working electrode. The counter and reference electrode is a polished magnesium foil and wire (Nilaco) respectively. The magnesium foil was polished by slide glass to remove the native oxide layer at the surface of the electrode just before usage in an argon filled glove box, whose atmosphere is controlled < 0.1 ppm of water content. The potential range of the CV measurement for the EAC electrolyte solution was between -1.0 and 2.0 V vs. Mg quasi-reference electrode, at the sweep rate 25 mV sec^{-1}. In the case of the BuMeG3 electrolyte solution, the CV measurement was taken between -2.4 and 2.0 V vs. Mg quasi-reference electrode, at 1 mV sec^{-1} of the sweep rate.

The galvanostatic electrodeposition was carried out with the same three-electrode cell as the CV measurements. The deposition current was 0.5 mA cm^{-2} for 6000 sec. The total electric charge for the magnesium deposition was 3 C cm^{-2} of cathodic current. After the galvanostatic electrodeposition process, the cells were disassembled and the platinum electrodes were rinsed with anhydrous dimethoxyethane (DME, Sigma Aldrich). The characterization of the electrodeposited magnesium was carried out using X-ray

diffraction (XRD, Rigaku, RINT2500). The surface morphologies of the electrodeposited magnesium were observed using a field emission SEM (Hitachi, S-4800).

2-3. ***Surface analyses***

The surface analyses were carried out using *in-situ* FTIR spectroscopy and X-ray photoelectron spectroscopy (XPS). In order to obtain the *in situ* FTIR spectra, we developed a diamond ATR-based *in situ* FTIR cell as shown in Fig. 2. A standard laboratory FTIR spectrometer (Nicolet^{TM} iS^{TM}50 FTIR, ThermoFisher Scientific) with an MCT-detector was employed for the spectroscopic measurement. The Pt thin film electrode was deposited on a commercial diamond-ATR disc (DuraSamplIR, Smiths Detection) using DC sputtering coater, and the *in situ* FTIR measurement was carried out by an internal reflection geometry. The counter and the reference electrodes were magnesium foil and wire, same as the normal electrochemical measurements. The infrared beam is introduced from the bottom of the diamond-ATR disc and focused at the diamond window. Total internal reflection of the infrared beam occurs at the surface of the diamond crystal with appearance of an evanescent wave, which typically has 0.5-1.0

μm penetration depth into the electrolyte solution to irradiates the molecules at the vicinity of the Pt thin film working electrode.

The *in situ* FTIR spectra were taken during CV measurements. The sweep rate of the CV is 0.2 mV sec^{-1} for both electrolyte solution. The potential range for the EAC electrolyte solution is between -0.4 and 1.0 V vs. Mg quasi-reference electrode. The potential range of the BuMeG3 electrolyte solution is between -1.4 and 1.0 V vs. Mg quasi-reference electrode. The lower potential limits of these CV measurements are set just above the onset electrode potential for the magnesium deposition.

Each FTIR spectrum was taken by the single beam mode with 512 of accumulation time. Subtractive normalized interfacial FTIR (SNIFTIR) spectrum was calculated by

$$\Delta R=(R_{n+1}-R_n)/R_n \qquad (1)$$

where R_n is a reference reflective spectrum and R_{n+1} is a reflective spectrum at a target electrode potential. Typical SNIFTIR spectrum has positive and negative peaks; the positive peaks are corresponding to the disappeared species at the vicinity of the electrode during the measurements of two spectra. The negative peaks are corresponding to the newly formed species such as surface layer formed at the surface of the electrode.

Adsorption and desorption process of the chemical species of the electrolyte solution at the surface of the electrode could also be appeared in the SNIFTIR spectra.

XPS was carried out to analyze the surface layer remained at the surface of the magnesium metal. Prior to the XPS measurements, the magnesium foils were also polished with slide glass in the glove box, to remove the native passivation layer. Subsequently, the magnesium foils were immersed in either the EAC electrolyte solution or the BuMeG3 electrolyte solution for 24 hours. The magnesium samples were rinsed with DME and dried under vacuum.

The prepared samples were placed in a transfer vessel in the glove box. The vessel was connected to the sample introduction chamber of the XPS and evacuated the chamber < 1.0 Pa for five minutes. The introduction chamber was subsequently filled with dried argon gas, then the samples were transferred into the introduction chamber. The XPS measurements were carried out with a standard XPS (Shimadzu. ESCA 3400) with Mg-Kα radiation. The emission current and the acceleration voltage of the X-ray Gun is 20 mA and 10 kV respectively. Depth profiles were taken by argon sputtering with the ion gun of emission currents: 20 mA and acceleration voltage: 2 kV. The etching rate is >

40 Å min^{-1} based upon SiO_2 and the etching time was 0, 10, 30, 30, 60, 300, 600, 1200, 1800 and 2400 sec.

3. Results and Discussion

3-1. *Comparison of the electrochemical behavior of magnesium deposition-dissolution*

Fig. 3 shows the cyclic voltammograms (CVs) of the magnesium deposition-dissolution processes in the EAC electrolyte solution and the BuMeG3 solution. The both CVs showed good agreement with results reported in elsewhere [19,22]. In the case of the EAC electrolyte solution, the overpotential of CV was approximately 0.34 V, while the overpotential of the ionic electrolyte solution was 1.66 V; this value is extremely large for battery applications. Furthermore, the ionic electrolyte solution showed a poor coulombic efficiency of 60 % was observed for the ionic electrolyte solution, as illustrated in the inset of Fig.3 (b), while the EAC electrolyte solution showed 99.7 % of the coulombic efficiency (inset of Fig. 3 (a)). The poor coulombic efficiency of the ionic electrolyte solution in Fig. 3 (b) suggests that the cathodic current is corresponding not only to the deposition of the magnesium metal but also to the reduction of the electrolyte

solution. The low current density for the deposition/dissolution process in the ionic electrolyte solution suggests that the activity of the Mg^{2+} ion is low, compared with the EAC electrolyte solution. Both of two oxidation peaks in the ionic electrolyte solution are corresponding to the dissolution of the magnesium metal. We think preferred orientation of the deposited magnesium particle could be a possible reason for the two peaks, because the crystal growth or the electrodeposited magnesium metal along *c* axis: [001], is slower than that of *a*/*b* axis: [100] or [110], as we previously reported [6]. In this case two types of the magnesium metal particles having different preferred orientation, could have been deposited. Another possibility is formation of inhomogeneous surface layer of the deposited magnesium. The deposited magnesium could be partially covered with high resistive layer via the reduction of the electrolyte solution. Further characterization of the deposited magnesium is necessary to understand the unique dissolution process of the magnesium metal.

Fig.4 (a) and (b) show SEM images of the magnesium films deposited in the EAC electrolyte solution and the BuMeG3 solution. In the case of the EAC electrolyte solution, a dense magnesium film with a smooth surface morphology was deposited as

shown in Fig. 4 (a). The magnified image shown in the inset of Fig. 4 (a), shows hexagonal-shaped grains, which probably reflects the hexagonal close packing structure of the magnesium metal[25]. On the other hand, the surface morphology of the magnesium deposited in the ionic electrolyte solution shows a surface morphology with aggregated spherical particles with small dimples. Furthermore, the deposited magnesium film is porous and not uniform, thus the Pt substrate is partially observed beneath the aggregated magnesium particles.

The XRD patterns of the magnesium films, deposited in the EAC electrolyte solution and the BuMeG3 solution, are shown in the Fig. 5. Both of the diffraction patterns well matched with the simulated powder pattern of magnesium metal from the database (ICDD pdf 00-035-0821). Since the XRD pattern of the magnesium film deposited in the EAC electrolyte solution has sharp peaks, the electrodeposited magnesium film is highly crystalline. On the other hand, the XRD pattern of the electrodeposited magnesium film in the BuMeG3 solution had relatively broad peaks, suggesting that the deposited magnesium has poor crystallinity[26]. Furthermore, the XRD pattern of the magnesium metal deposited in BuMeG3 normalized with 101

reflection peaks observed at 36.5 º of 2θ. It suggests that the amount of the deposited magnesium is not as much as that of EAC electrolyte solution, because of the low S/N ratio of the diffraction pattern. The poor coulombic efficiency with the small amount of deposited magnesium metal, suggests that some side reactions such as the reduction of the electrolyte solution, took place during the electrodeposition process in the BuMeG3 solution. The side reaction may hinder the smooth crystal growth process of the magnesium.

Generally, it is considered that the surface films are not formed at the surface for reversible magnesium deposition-dissolution process, because the magnesium metal easily forms passivation layer with no ionic conductive properties. The EAC electrolyte solution is a typical example of the passivation-free electrolyte solution, as a consequence the EAC electrolyte solution shows approx. 100% of the coulombic efficiency during the deposition-dissolution process. On the other hand, a surface layer is probably formed in the BuMeG3 electrolyte solution, because it shows poor coulombic efficiency.

3-2. ***Investigation of the decomposed electrolyte solution during the reduction-***

oxidation process

In order to confirm the reduction process of the electrolyte solutions, we conducted *in situ* FTIR spectroscopy and XPS. Fig. 6 shows a series of *in situ* FTIR spectra of the EAC electrolyte solution during CV measurements. The CV measurement for the *in situ* FTIR was carried out between -0.4 and 1.2 V vs. Mg quasi-reference electrode, and the sweep rate was 0.2 mV sec^{-1}. The lower potential limit of the CV needs to be above the onset electrode potential of magnesium deposition, because it is necessary to maintain the thickness of the working electrode enough thin. Otherwise, the incident infrared beam is reflected by the deposited magnesium metal, as a consequence, the evanescent wave the electrode-electrolyte interphase.

The *in situ* FTIR spectra observed strong peaks corresponding to the structural changes even at high electrode potential >0.5 V vs. Mg quasi-reference electrode. Several positive and negative peaks around 1078-860 cm^{-1} are corresponding to THF molecules. The positive peaks at 1062 and 1025 cm^{-1} are assigned to the antisymmetric and symmetric C-O-C stretching vibration, the positive peaks at 899 and 854 cm^{-1} are assigned to the CH_2 wagging vibration of THF. The negative peak observed at 1078 cm^{-}

[1] is corresponding to the ν C-O-C stretching vibration of THF molecules at the surface of the electrode. These spectrum changes are continuously observed during the cathodic scan of the CV measurement, suggesting that the THF molecules continuously form a surface layer until the electrode potential reaches at -0.4 V vs. Mg quasi-reference electrode. A summary of the peak assignment for the *in situ* FTIR spectra for the EAC electrolyte solution is shown in Table 1[23].

The *in situ* FTIR spectra for the 1st anodic scan are also shown in Fig. 6 (a). Since the *in situ* FTIR spectra at the beginning of the anodic scan did not show clear peaks, the adsorbed molecules seem to remain at the surface of the electrode. As the electrode potential reaches to more positive >1.0 V vs. Mg quasi-reference electrode, some spectrum changes were observed. The *in situ* FTIR spectrum at more positive electrode potential showed a flipped shape of the spectrum during the cathodic scan, thus we think the surface layer in the EAC electrolyte is based upon an adsorption or a structural reformation of the THF molecules at the vicinity of the electrode. Since the surface layer is not formed by the irreversible decomposition of the electrolyte solution, the EAC electrolyte maintains a dynamic reversible interphase. In the following CV cycle,

almost same reversible spectra changes are detected as shown in Fig. 6 (b). The peaks are most clearly observed at -0.4 and 1.5 V vs Mg quasi-reference electrode during the cathodic and the anodic scan respectively. This overpotential for the reversible spectrum changes could be related with the formation process of the intermediate species of Mg deposition such as decomposed Mg dimer species reported in the past [16].

Fig. 7 shows SNIFTIR spectra of the electrolyte solution: 0.5 M $Mg(TFSA)_2$ in BuMeG3 during the CV measurement. In this case, the CV measurement was scanned between 1.2 and -1.4 V vs. Mg quasi-reference electrode, which is the electrode potential range just above the magnesium deposition occurs. The sweep rate of the CV measurement was 0.2 mV sec^{-1} as well. During the 1st cathodic scan, several positive and negative peaks were observed at 0 V vs. Mg quasi-reference electrode and more negative electrode potential. The positive peaks at 1346, 1328, 1041, 919 cm^{-1} are assigned to SO_2 and the peaks at 1182, 759 cm^{-1} are assigned to CF_3 in TFSA anion respectively. Those peaks were continuously observed until the electrode potential reached to the lower potential limit. Table 2 shows a summary of the peak assignments for the BuMeG3 electrolyte solution. Subsequently SNIFTIR spectra for the 1st anodic

scan was taken, however, almost no clear peaks were observed during the anodic scan up to the open circuit potential suggesting that a stable surface layer was formed during the 1st cathodic scan. Furthermore, the SNIFTIR spectra for the 2nd CV measurement shows even more flat spectra both cathodic and anodic sweep. We think the surface layer on the Pt thin film electrode during the 1st cathodic scan is not like the surface layer so-called "solid electrolyte interphase (SEI) layer" but a "passivation layer", because the Pt thin film electrode seems to be mostly inactive. Since most of the peaks observed in the SNIFTIR spectra for the 1st cathodic scan in the BuMeG3 electrolyte are corresponding to the TFSA anion, the decomposed species should be remained as a surface film of the electrode. Moreover, we think the high overpotential for the magnesium deposition/dissolution process could be due to the passivation layer formed in the BuMeG3 electrolyte solution.

3-3. *Characterization of the surface film on magnesium metal using XPS*

XPS analyses for magnesium metal were carried out to characterize the surface layer. In order to take depth profiles of the surface layer on magnesium metal, an argon ion

sputtering was subsequently carried out after each XPS measurement, thus several stacked spectra are shown in one graph. In the XPS spectra, the top spectrum is corresponding to the very surface and the bottom as bulk. Fig. 8 shows the XPS spectra of an as-prepared magnesium foil. The magnesium foil was polished with a slide glass to remove the native passivation layer in an argon filled glove box before the XPS measurement. The Mg 2p spectra for the as-prepared magnesium foil have a broad peak, which obviously consists of two overlapped peaks at 49.6 eV and 51.0 eV. The two peaks at 49.6 eV and 51.0 eV are corresponding to magnesium metal and magnesium oxide respectively. The peak intensity of magnesium and magnesium oxide slightly increased by argon ion sputtering. The O 1s XPS spectra for the as-prepared magnesium foil are shown in Fig. 8 (b). Each spectrum also has two overlapped peaks at 531.2 eV and 532.8 eV, corresponding to magnesium oxide and C-O-C bond of organic species respectively. The peaks observed at 286.0 eV and 290.2 eV of C1s spectra are assigned to ether and carbonate respectively. Since the as prepared magnesium foil was polished just before the XPS measurement, the organic species at the surface should be the contamination from the glove box atmosphere. The surface organic species could be the

reacted species of the solvent molecules such as THF or DME, evaporated in the glove box. Furthermore, it is obvious that the bulk magnesium foil contains considerable amount of MgO.

The XPS spectra of a magnesium foil immersed in the organohaloaluminate-based electrolyte solution: Ethyl magnesium chloride and diethyl Aluminum Chloride (EAC) electrolyte is shown in the Fig. 9. Overall the spectra are similar to the spectra for the as-prepared magnesium foil. The Mg 2p spectra of the magnesium also have two peaks; one corresponding to magnesium metal at 49.6 eV, and another to magnesium oxide at 51.0 eV. The magnesium oxide was also detected in the O 1s XPS spectra at 531.2 eV. The peak corresponding to C-O-C bond is also observed at 532.8 eV. The C 1s XPS spectra also have peaks assigned to C-O-C bond, and a very small peak of magnesium carbonate. A broad peak is observed in the Cl 2p spectra at 199 eV, suggesting that a magnesium dimer complex formed in the EAC electrolyte adsorbed at the surface of the magnesium. However, the amount of the remaining Cl species is very small. Thus, we think that the XPS spectra do not show clear evidence of the decomposition of the EAC electrolyte at the surface of the magnesium metal, but they show some residual of

the electrolyte. These results are in good agreement with the *in situ* FTIR spectra discussed in the previous section.

Fig. 10 shows the XPS spectra of a magnesium foil immersed in the ionic electrolyte solution: 0.5 M $Mg(TFSA)_2$ in BuMeG3. At glance, the Mg 2p spectra of the magnesium foil, immersed in the ionic electrolyte, are similar to that of the above two samples. Two peaks corresponding to magnesium metal and MgO are observed as well. Since MgF_2 should be observed around 51.9 eV in the Mg 2p spectra, the XPS peak for the MgO could be overlapped with MgF_2. O 1s spectra also have two overlapped peaks. One at 531.2 eV is corresponding to magnesium oxide, another at 532.8 eV is assigned to C-O-C bond of the solvent molecules. In this case the peak intensity of the C-O-C bond remains strong even after the long argon sputtering process. The C 1s spectra show new peak at 293.8 eV corresponding to C-F bond at the very surface of the magnesium foil. It suggests that the TFSA anion or its derivative is remaining as a residue of the ionic electrolyte solution. The F 1s XPS spectra shown in Fig. 10 (d), also have a strong peak corresponding to the TFSA anion at 689.5 eV. During the argon sputtering process, the peak at 689.5 eV gradually disappeared and another peak appeared at 686.2 eV.

Though the typical F 1s XPS peak corresponding to MgF_2 should be appeared around 685.7 eV, we think the peak at 686.2 eV is probably corresponding to MgF_2, because many metal fluorides have peaks around 686.0 eV and fluorinated alkyl groups typically have peaks around 689 eV. The formation of MgF_2 clearly shows the decomposition of TFSA anion at the surface of the magnesium metal.

Through the comparison of the XPS spectra for the three samples, the MgF_2-based passivation layer formed via decomposition of the TFSA anion, causes the high overpotential of the deposition / dissolution process of magnesium metal due to the poor electric and ionic conductive prorperties of MgF_2[27]. The decomposition of the electrolyte also hinders the crystal growth of the magnesium metal during the deposition process, resulting in the poor crystallinity. Thus, we think the decomposition of the electrolyte solution needs to be suppressed for the smooth electrochemical deposition / dissolution process of the magnesium metal.

4. Conclusion

In the present study, we compared the electrochemical properties of magnesium metal using the EAC electrolyte solution and the ionic electrolyte solution. The EAC electrolyte solution showed relatively low overpotential approximately 0.34 V, while the ionic electrolyte solution showed very high overpotential >1.5 V. The coulombic efficiency of the EAC electrolyte solution and the ionic electrolyte solution were 99.7 % and approximately 60 % respectively. The magnesium metal deposited in the ionic electrolyte solution showed poor crystallinity due to the reduction of the electrolyte solution during the deposition process. The passivated surface of the deposited magnesium metal via decomposition of the electrolyte solution, hinders the smooth crystal growth of the magnesium. The decomposition process of the electrolyte solutions was analyzed using *in situ* FTIR spectroscopy. The *in situ* FTIR spectra for the EAC electrolyte solution was highly reversible during the CV measurement, suggesting that the surface of the Pt electrode was not passivated. On the other hand, the *in situ* FTIR spectra for the ionic electrolyte solution showed several peaks only at the 1st cathodic scan and no peaks during the following scans. It shows that the electrode

surface is passivated during the 1st cathodic scan. Furthermore, the XPS spectra for the magnesium metal immersed in the ionic electrolyte solution proved that TFSA anion in the ionic electrolyte solution was decomposed at the surface of the magnesium metal, resulting in the formation of MgF_2-based passivation layer. Therefore, the high overpotential of the magnesium deposition / dissolution process in the ionic electrolyte solution is caused by the formation of the passivation layer via decomposition of the TFSA anion. We think finding novel anion species with improved reductive stability such as monocarborane[24] is very crucial for further development of rechargeable magnesium batteries.

Acknowledgement

The present study was financially supported by Japan Science and Technology Agency PRESTO (Grant No. JPMJPR13CA)

Figure Captions

Fig. 1 Schematic representative of the three-electrode cell used in the present study

Fig. 2 Schematic representative of the diamond ATR-based *in situ* FTIR cell used in the present study

Fig. 3 Cyclic voltammograms for the deposition-dissolution processes of the Mg metals in the 0.25 M EtMgCl-2Et_2AlCl in THF (a) and the 0.5 M $Mg(TFSA)_2$ in BuMeG3 (b)

Fig. 4 SEM images of the Mg metals deposited on the Pt substrates in the 0.25 M EtMgCl-2Et_2AlCl in THF solution (a) and the 0.5 M $Mg(TFSA)_2$ in BuMeG3 solution (b)

Fig. 5 X-ray diffraction patterns of the electrodeposited Mg metals on the Pt substrates in the 0.25 M EtMgCl-2Et_2AlCl in THF solution (a) and the 0.5 M $Mg(TFSA)_2$ in BuMeG3 solution (b) with a reference diffraction pattern (#ICDD 00-035-0821)

Fig. 6. *in-situ* FTIR spectra of a CV measurement using a Pt thin film electrode formed on the diamond window in 0.25 M EtMgCl-2Et_2AlCl in THF solution, between the open circuit potential (1.32 V vs. Mg quasi-reference electrode) and -0.4 V vs. Mg quasi-reference electrode, during the 1st CV cycle (a), and the 2nd cycle (b)

Fig. 7. *in-situ* FTIR spectra of a CV measurement using a Pt thin film electrode formed on the diamond window in 0.5 M $Mg(TFSA)_2$ in BuMeG3 solution, between the open circuit potential (1.15 V vs. Mg quasi-reference electrode) and -1.4 V vs. Mg quasi-reference electrode, during the 1st CV cycle (a), and the 2nd cycle (b)

Fig. 8. Groups of the XPS spectra for the as prepared Mg metal; Mg 2p (a), O 1s (b), and C 1s (c). The spectrum at the top of the graph corresponds to the very surface of the sample. The following spectra were taken after the Ar ion beam sputtering. The

sputtering time is noted at the right side of each spectrum

Fig. 9. Groups of the XPS spectra for the Mg metal immersed in the 0.25 M EtMgCl-2Et_2AlCl in THF; Mg 2p (a), O 1s (b), C 1s (c) and Cl 2p (d). The Ar ion beam sputtering times are noted at the right side of the graph

Fig. 10. Groups of the XPS spectra for the Mg metal immersed in the 0.5 M $Mg(TFSA)_2$ in BuMeG3; Mg 2p (a), O 1s (b), C 1s (c) and F 1s (d). The Ar ion beam sputtering times are noted at the right side of the graph.

References

1. W. M. Besenhard J.O., *Chem. Phys. Chem.*, **3**, 155 (2002).
2. K. Ariyoshi, R. Yamato and T. Ohzuku, *Electrochimica Acta*, **51**, 1125 (2005).
3. J.-M. Tarascon and M. Armand, *Nature*, **414**, 359 (2001).
4. R. J. Hoffman, T. D. Gregory and R. C. Winterton, *Journal of The Electrochemical Society*, **137**, 775 (1990).
5. D. Aurbach, A. Schechter, M. Moshkovich and Y. Cohen, *Journal of The Electrochemical Society*, **148**, A1004 (2001).
6. M. Matsui, *Journal of Power Sources*, **196**, 7048 (2011).
7. Z. Lu, A. Schechter, M. Moshkovich and D. Aurbach, *Journal of Electroanalytical Chemistry*, **466**, 203 (1999).
8. D. Aurbach, I. Weissman, Y. Gofer and E. Levi, *Chem Rec*, **3**, 61 (2003).
9. L. W. Gaddum and H. E. French, *Journal of the American Chemical Society*, **49**, 1295 (1927).
10. D. Aurbach, A. Lu, A. Schechter, Y. Gofer, H. Gizbar, R. Turgeman, Y. Cohen, M. Moshkovich and E. Levi, *Nature*, **407**, 724 (2000).
11. D. Aurbach, Y. Gofer, A. Schechter, O. Chusid, H. Gizbar, Y. Cohen, M. Moshkovich and R. Turgeman, *Journal of Power Sources*, **97-98**, 269 (2001).
12. R. T. Yossi Gofer, H. Cohen, and Doron Aurbach, *Langmuir*, **19**, 2344 (2003).
13. O. C. Yulia Vestfried, Yossi Goffer, Pinchas Aped, and Doron Aurbach, *Organometallics*, **26**, 3130 (2007).
14. D. Aurbach, G. S. Suresh, E. Levi, A. Mitelman, O. Mizrahi, O. Chusid and M. Brunelli, *Advanced Materials*, **19**, 4260 (2007).
15. O. Mizrahi, N. Amir, E. Pollak, O. Chusid, V. Marks, H. Gottlieb, L. Larush, E. Zinigrad and D. Aurbach, *Journal of The Electrochemical Society*, **155**, A103 (2008).
16. H. S. Kim, T. S. Arthur, G. D. Allred, J. Zajicek, J. G. Newman, A. E. Rodnyansky, A. G. Oliver, W. C. Boggess and J. Muldoon, *Nat Commun*, **2**, 427 (2011).
17. J. Muldoon, C. B. Bucur, A. G. Oliver, T. Sugimoto, M. Matsui, H. S. Kim, G. D. Allred, J. Zajicek and Y. Kotani, *Energy & Environmental Science*, **5**, 5941 (2012).
18. S. Yagi, A. Tanaka, Y. Ichikawa, T. Ichitsubo and E. Matsubara, *Journal of The Electrochemical Society*, **160**, C83 (2013).
19. T. Fukutsuka, K. Asaka, A. Inoo, R. Yasui, K. Miyazaki, T. Abe, K. Nishio and Y. Uchimoto, *Chemistry Letters*, **43**, 1788 (2014).

20. S. Y. Ha, Y. W. Lee, S. W. Woo, B. Koo, J. S. Kim, J. Cho, K. T. Lee and N. S. Choi, *ACS Appl Mater Interfaces*, **6**, 4063 (2014).
21. Y. Orikasa, T. Masese, Y. Koyama, T. Mori, M. Hattori, K. Yamamoto, T. Okado, Z. D. Huang, T. Minato, C. Tassel, J. Kim, Y. Kobayashi, T. Abe, H. Kageyama and Y. Uchimoto, *Sci Rep*, **4**, 5622 (2014).
22. A. Benmayza, M. Ramanathan, T. S. Arthur, M. Matsui, F. Mizuno, J. Guo, P.-A. Glans and J. Prakash, *The Journal of Physical Chemistry C*, **117**, 26881 (2013).
23. R. T. D. Aurbach, O. Chusid, Y. Gofer, *Electrochemistry Communications*, **3**, 252 (2001).
24. O. Tutusaus, R. Mohtadi, T. S. Arthur, F. Mizuno, E. G. Nelson and Y. V. Sevryugina, *Angew Chem Int Ed Engl*, **54**, 7900 (2015).
25. A. W. Hull, *Physical Review*, **10**, 661 (1917).
26. B. D. Culity, *Elements of X-ray Diffraction*, Addison Wesley Pub., Reading , Massachusetts (1978).
27. D. N. Karimov, N. I. Sorokin, S. P. Chenov and B.P. Sobelev, *Crystallography Reports*, **59**, 928 (2014).

Table 1 Summary of the peak assignments of the *in situ* FTIR spectra for the 0.25 M EtMgCl-2Et_2AlCl in THF solution during the 1st cathodic scan

cm^{-1}	
	Positive Peaks
1062	C-O-C asymmetric stretching vibration of free THF
1025	C-O-C asymmetric stretching vibration of solvated THF
899	C-H wagging vibration of THF
854	C-H wagging vibration of THF
	Negative Peaks
1074	C-O-C asymmetric stretching vibration of adsorbed THF
921	C-H bending vibration of adsorbed THF

Table 2 Summary of the peak assignments of the *in situ* FTIR spectra for the 0.5 M $Mg(TFSA)_2$ in BuMeG3 solution during the 1st cathodic scan

cm^{-1}	
	Positive Peaks
1346	O=S=O bending vibration of the TFSA anion
1328	O=S=O bending vibration of the TFSA anion
1182	Antisymmetric CF_3 stretching vibration of the TFSA anion
1100	C-O-C antisymmetric stretching vibration of the BuMeG3
1051	S-N-S stretching vibration of the TFSA anion
1041	O=S=O symmetric stretching vibration of the TFSA anion
979	C-O-C symmetric stretching vibration of the BuMeG3
919	O=S=O symmetric stretching vibration of the TFSA anion
782	C-S stretching vibration of the TFSA anion
759	CF_3 bending vibration of the TFSA anion
736	CH_2 rocking vibration of the BuMeG3
	Negative Peaks
1361	O=S=O bending vibration of the decomposed TFSA anion
1209	Antisymmetric CF_3 stretching vibration of the decomposed TFSA anion
1149	C-O-C antisymmetric stretching vibration of the adsorbed / decomposed BuMeG3
1083	S-N-S stretching vibration of the decomposed TFSA anion
1066	O=S=O symmetric stretching vibration of the decomposed TFSA anion

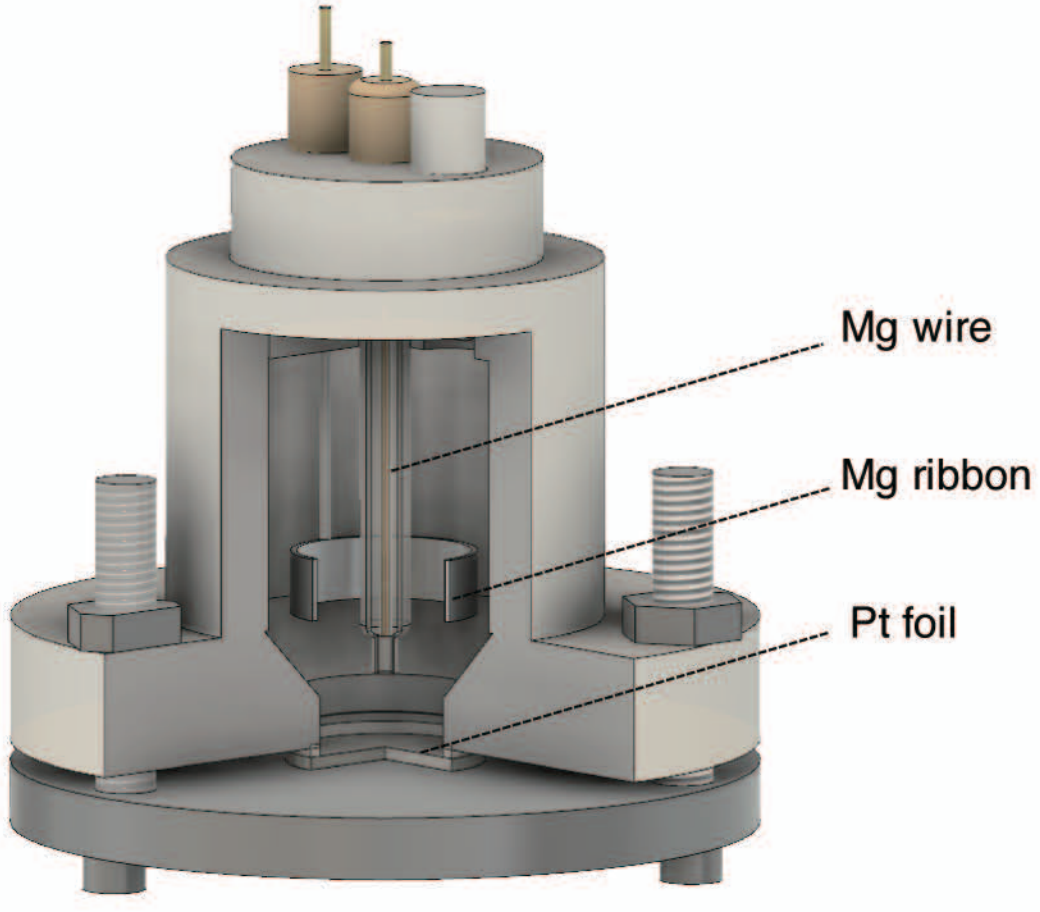

Fig. 1 Schematic representative of the three-electrode cell used in the present study

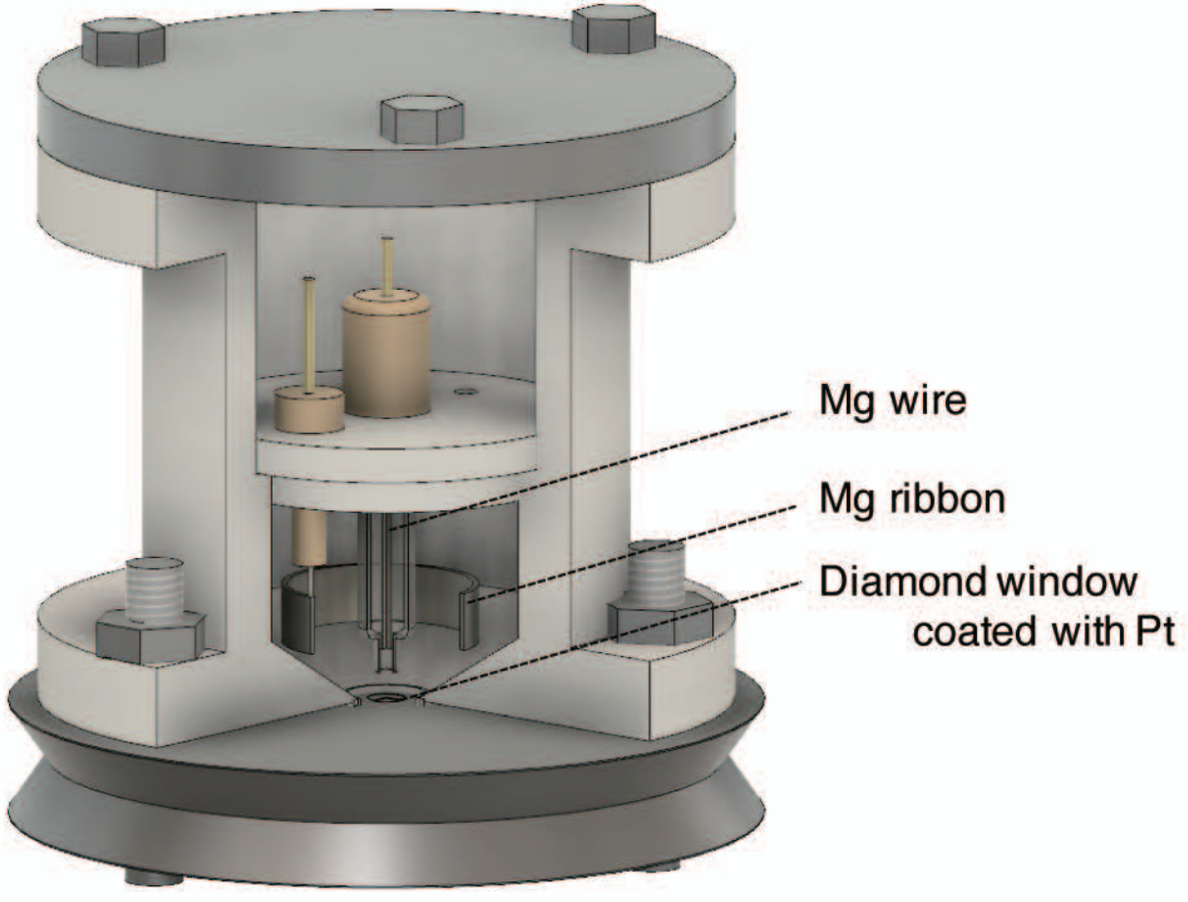

Fig. 2 Schematic representative of the diamond ATR-based *in situ* FTIR cell used in the present study

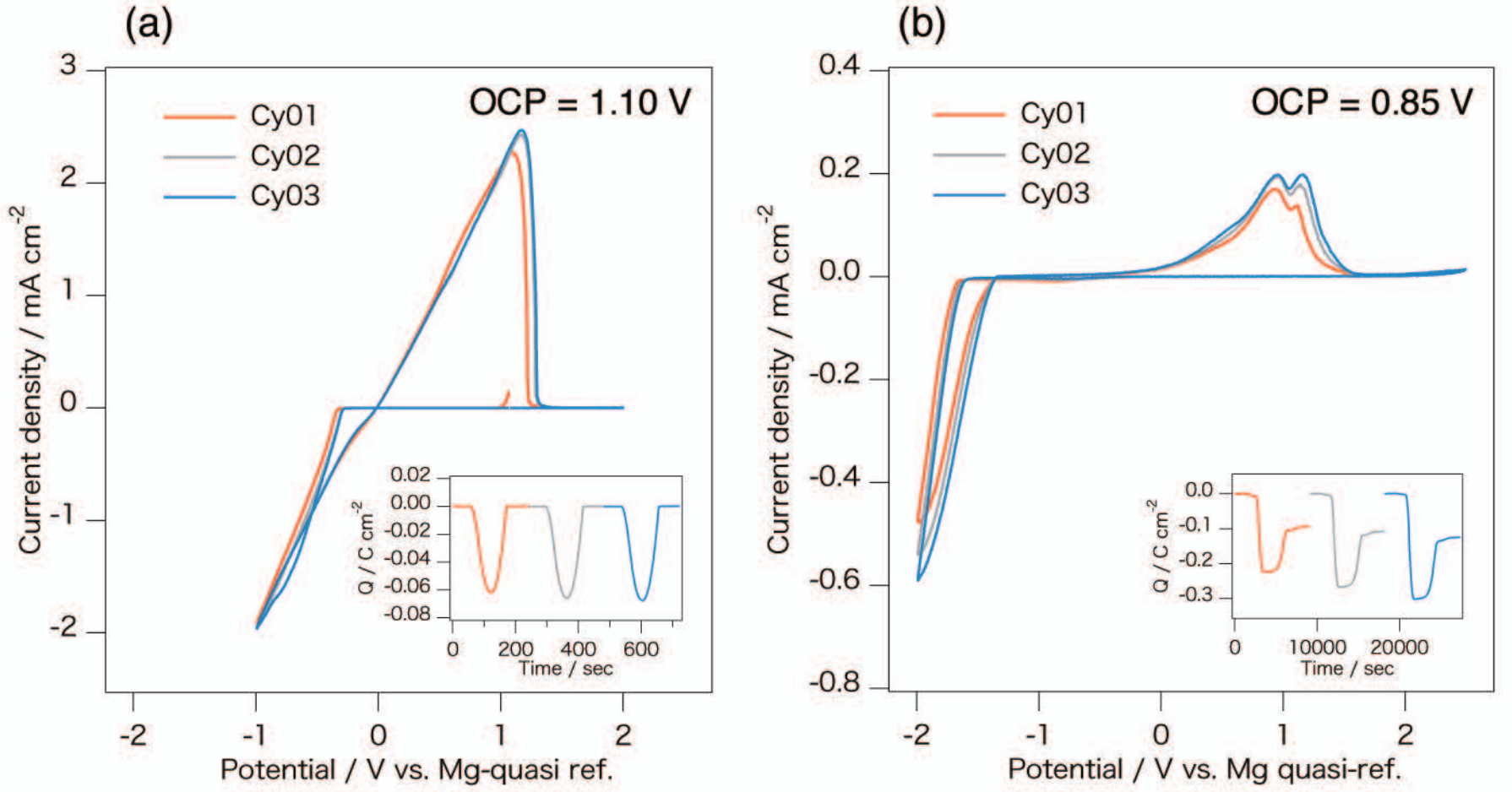

Fig. 3 Cyclic voltammograms for the deposition-dissolution processes of the Mg metals in the 0.25 M EtMgCl-2Et_2AlCl in THF (a) and the 0.5 M Mg(TFSA)$_2$ in BuMeG3 (b)

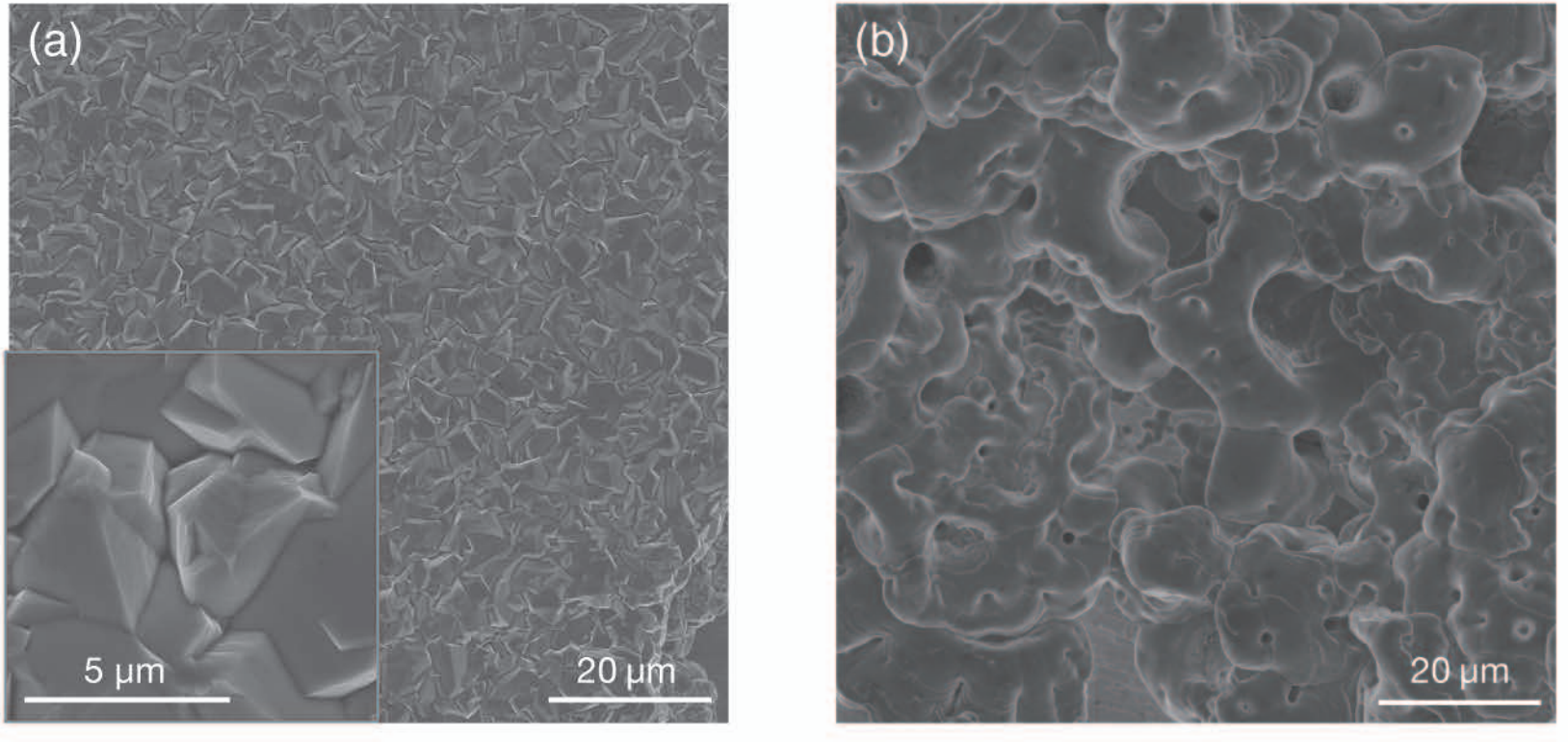

Fig. 4 SEM images of the Mg metals deposited on the Pt substrates in the 0.25 M EtMgCl-$2Et_2AlCl$ in THF solution (a) and the 0.5 M $Mg(TFSA)_2$ in BuMeG3 solution (b)

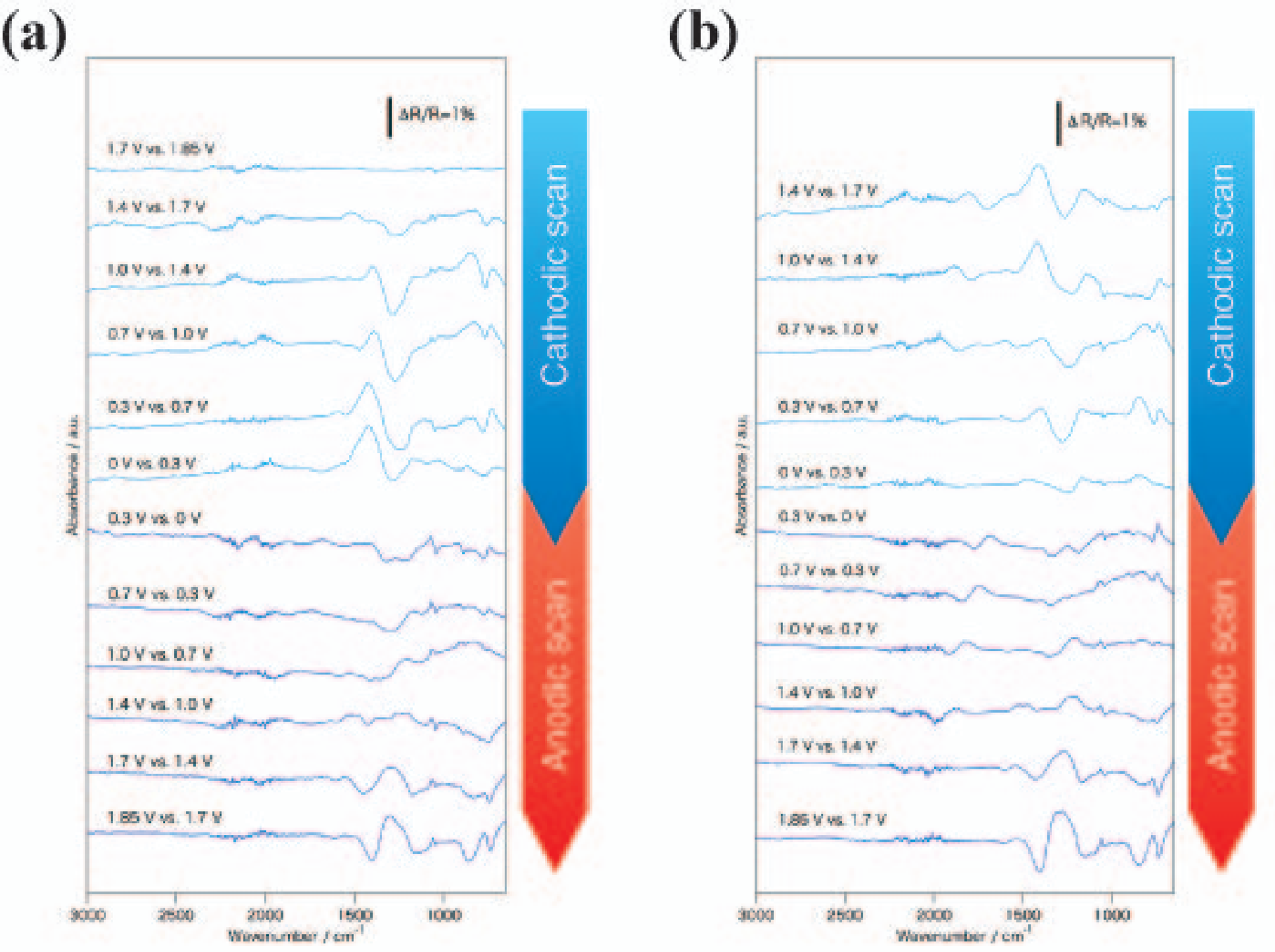

Fig. 5 *In situ* FTIR spectra of Ni thin film electrode in the $LiBH_4$-based electrolyte solution. The CV measurement was taken between the initial open circuit potential (OCP) and 0 V vs. Li/Li^+. The OCP is 1.85 V vs. Li/Li^+ for two cycles.

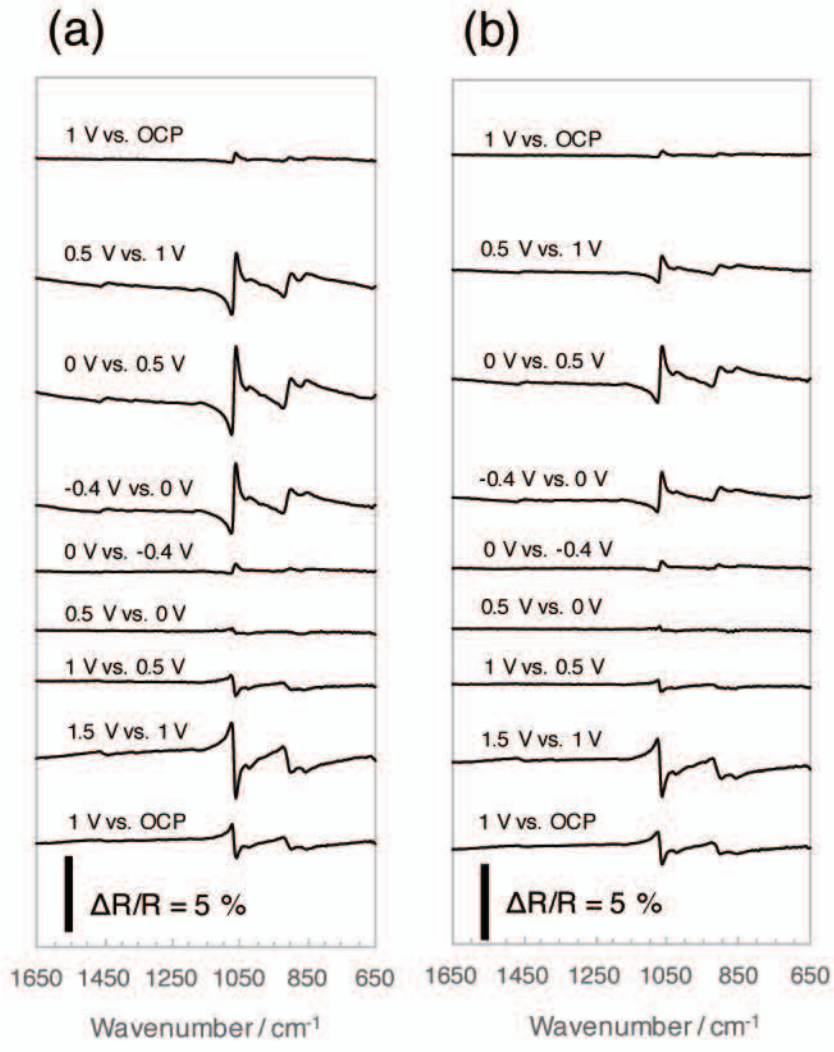

Fig. 6. *in-situ* FTIR spectra of a CV measurement using a Pt thin film electrode formed on the diamond window in 0.25 M EtMgCl-Et_2AlCl in THF solution, between the open circuit potential (1.32 V vs. Mg quasi-reference electrode) and -0.4 V vs. Mg quasi-reference electrode, during the 1st CV cycle (a), and the 2nd cycle (b)

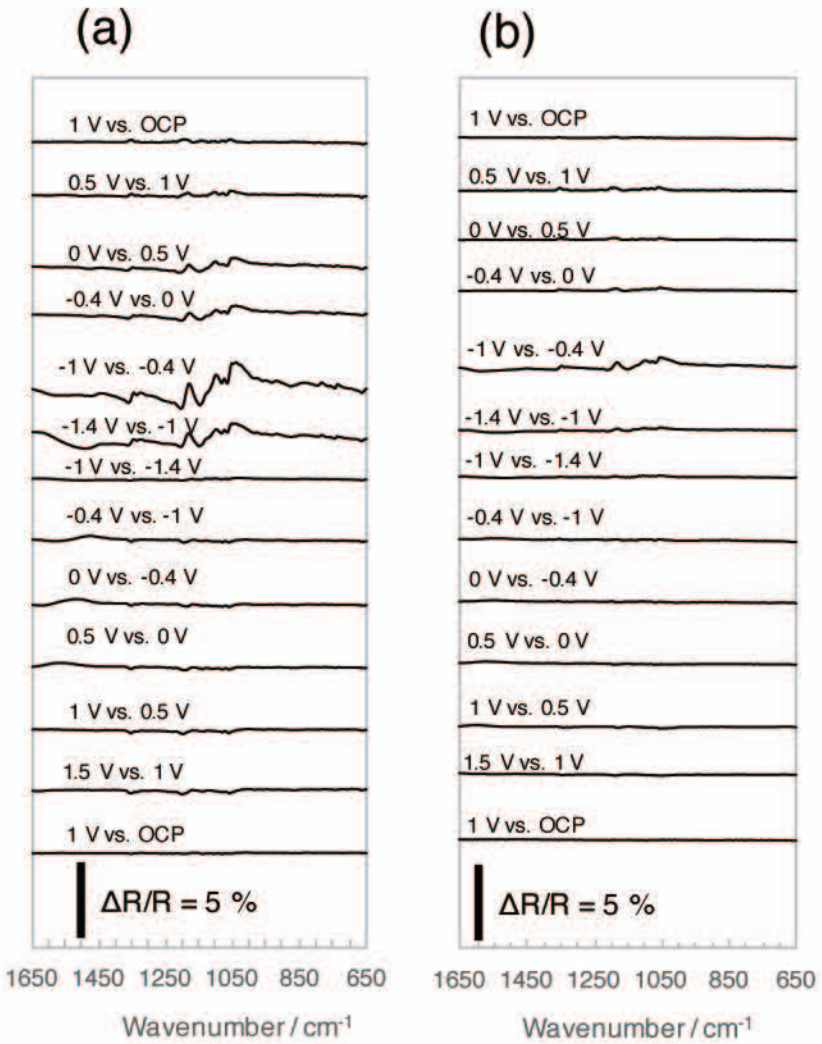

Fig. 7. *in-situ* FTIR spectra of a CV measurement using a Pt thin film electrode formed on the diamond window in 0.5 M $Mg(TFSA)_2$ in BuMeG3 solution, between the open circuit potential (1.15 V vs. Mg quasi-reference electrode) and -1.4 V vs. Mg quasi-reference electrode, during the 1st CV cycle (a), and the 2nd cycle (b)

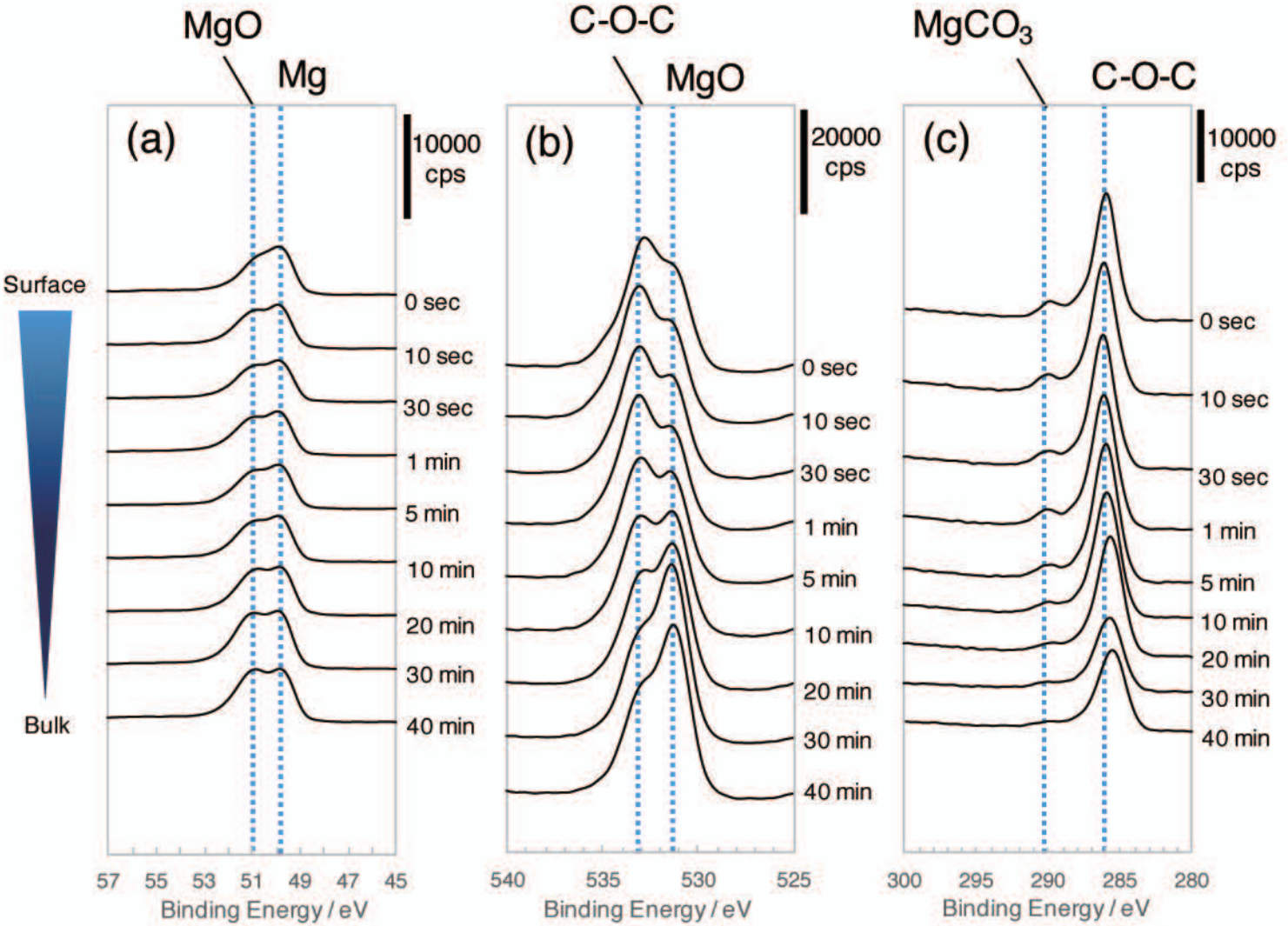

Fig. 8. Groups of the XPS spectra for the as prepared Mg metal; Mg 2p (a), O 1s (b), and C 1s (c). The spectrum at the top of the graph corresponds to the very surface of the sample. The following spectra were taken after the Ar ion beam sputtering. The sputtering time is noted at the right side of each spectrum

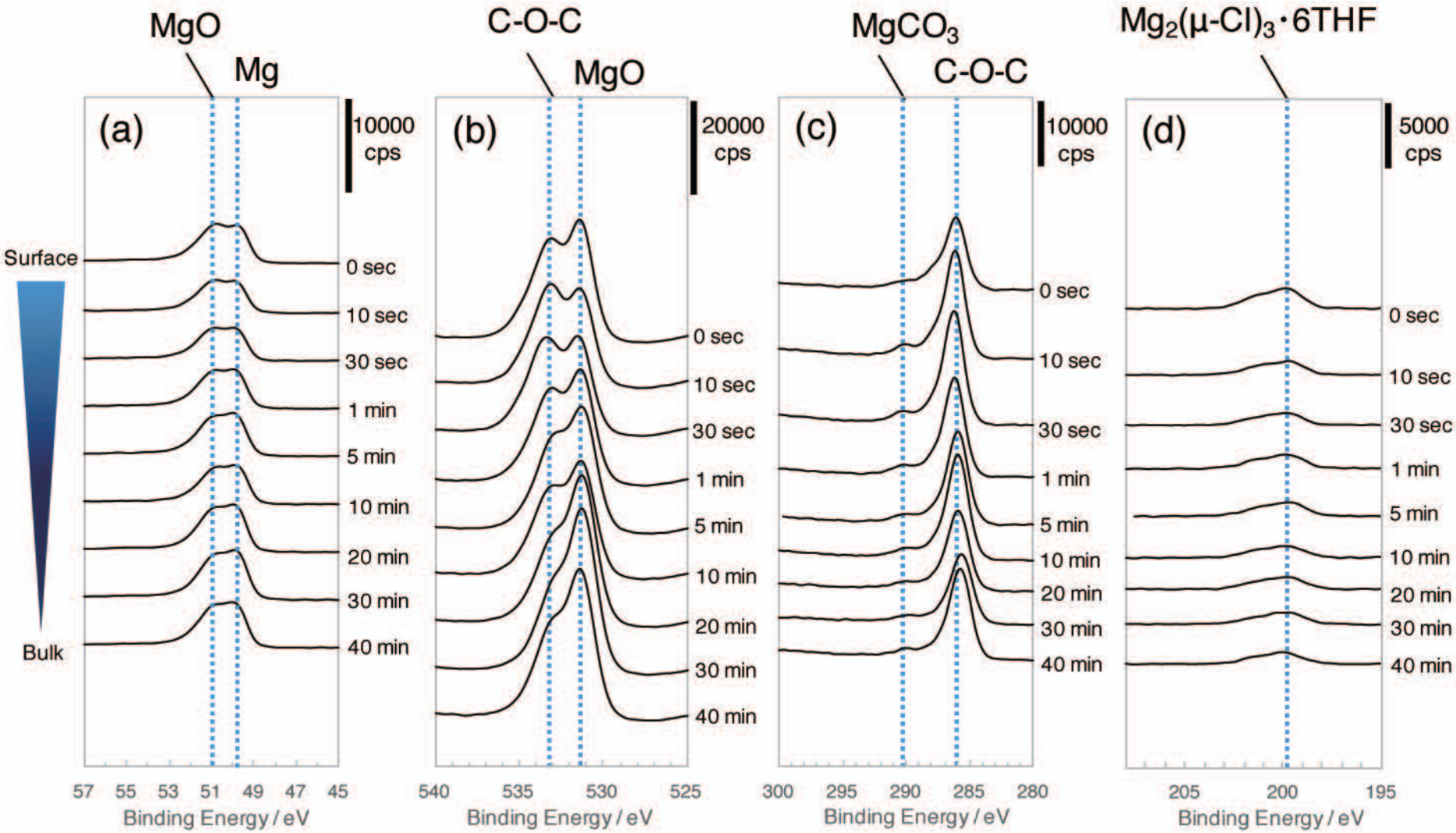

Fig. 9. Groups of the XPS spectra for the Mg metal immersed in the 0.25 M EtMgCl-Et_2AlCl in THF; Mg 2p (a), O 1s (b), C 1s (c) and Cl 2p (d). The Ar ion beam sputtering times are noted at the right side of the graph

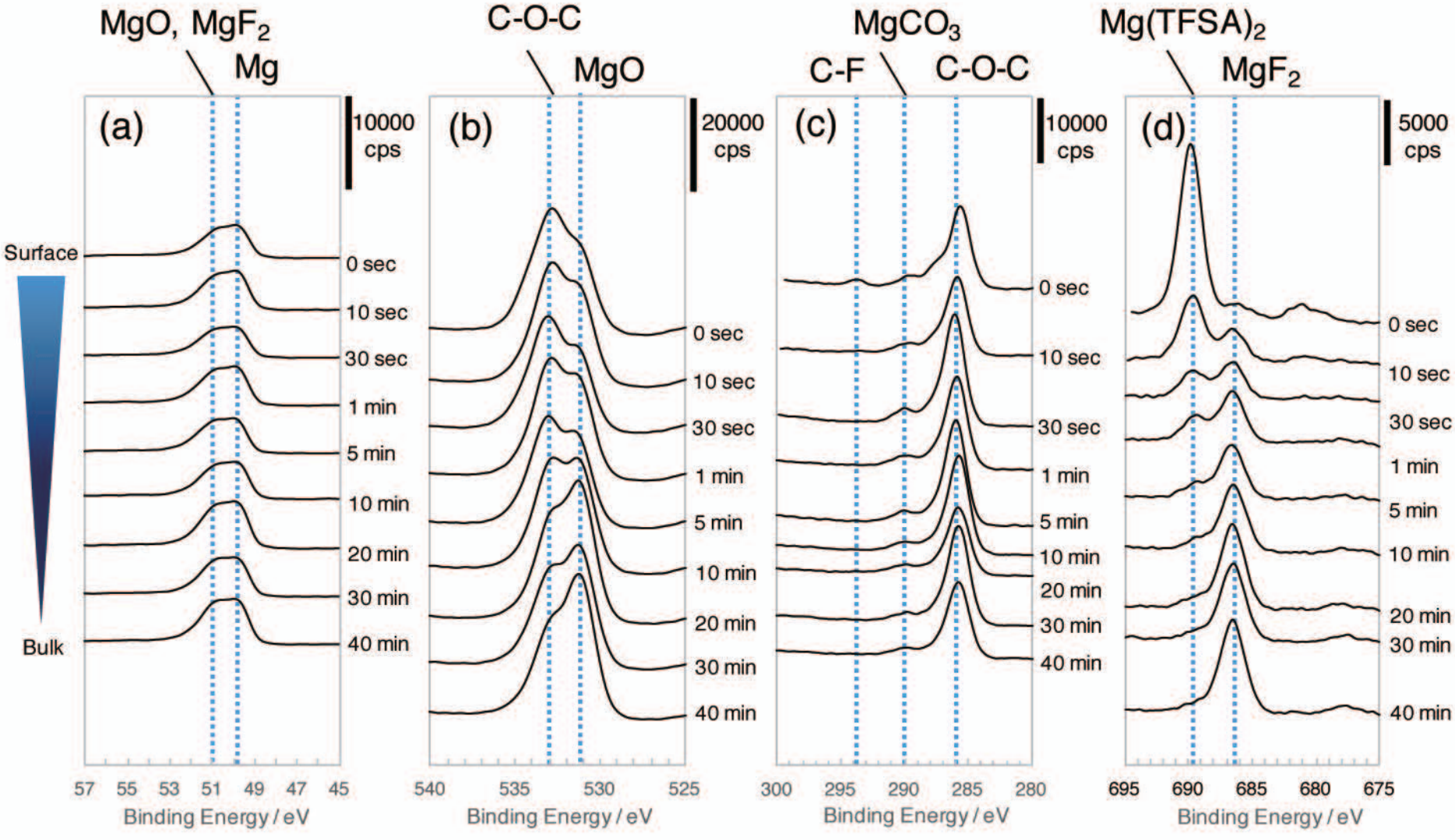

Fig. 10. Groups of the XPS spectra for the Mg metal immersed in the 0.5 M $Mg(TFSA)_2$ in BuMeG3; Mg 2p (a), O 1s (b), C 1s (c) and F 1s (d). The Ar ion beam sputtering times are noted at the right side of the graph